Passive Imaging of Hydrofractures in the South Belridge Diatomite

D.C. Ilderton,* SPE, **T.W. Patzek,** SPE, and **J.W. Rector,** U. of California; and **H.J. Vinegar,** SPE, Shell Development Co.

Summary

We present the results of a seismic analysis of two hydrofractures spanning the entire diatomite column (1110-1910 ft or 338-582 m) in Shell's Phase II steamdrive pilot in South Belridge, California. These hydrofractures were induced at two depths (1110-1460 and 1560-1910 ft) and imaged passively using the seismic energy released during fracturing. The arrivals of shear waves from the cracking rock ("microseismic events") were recorded at a 1 ms sampling rate by 56 geophones in three remote observation wells, resulting in 10GB of raw data. These arrival times were then inverted for the event locations, from which the hydrofracture geometry was inferred. A five-dimensional conjugate-gradient algorithm with a depth-dependent, but otherwise constant shear wave velocity model (CVM) was developed for the inversions. To validate CVM, we created a layered shear wave velocity model of the formation and used it to calculate synthetic arrival times from known locations chosen at various depths along the estimated fracture plane. These arrival times were then inverted with CVM and the calculated locations compared with the known ones, quantifying the systematic error associated with the assumption of constant shear wave velocity. We also performed Monte Carlo sensitivity analyses on the synthetic arrival times to account for all other random errors that exist in field data. After determining the limitations of the inversion algorithm, we hand-picked the shear wave arrival times for both hydrofractures and inverted them with CVM. Finally, to correct for the areal inhomogeneity of the rock, we calculated the distortion of conical waves that were generated by air gun blasts in a remote observation well. This novel technique improved significantly the accuracy of the event locations in the shallow hydrofracture. The azimuth of both hydrofractures was N21° ± 4°E. In each treatment well, there were two separate hydrofractures at two different depths that correspond to the diatomite layers with higher permeabilities. Both shallow hydrofractures were asymmetrical. Initially, the upper NE wing was 230 ft long, whereas the lower SW wing was only 30 ft long. The deep hydrofracture was symmetrical and the wings of its two parts were initially 130 and 10 ft long, respectively. These conclusions agree well with temperature surveys in the surrounding observation wells during steam injection.

Introduction

The late and middle Miocene diatomaceous oil fields in the San Joaquin Valley, California, are located in Kern County, some forty miles west of Bakersfield. The largest oil volumes are found in the South, Middle and North Belridge Diatomite and Brown Shale, Lost Hills Diatomite and Brown Shale, Antelope Hills, McDonald Anticline, Chico-Martinez Chert, Cymric Diatomite, McKittrick, Railroad Gap, Belgian Anticline, Asphalto, Elk Hills, Buena Vista Antelope Shale, and Midway Sunset Reef Ridge and Antelope Shale. The major producers of diatomite oil are Shell, Mobil, Chevron, Santa Fe, Crutcher Tufts, Exxon, Texaco, and Unocal. An estimated original-oil-in-place in the Monterey diatomaceous fields exceeds 10 billion barrels and is comparable to that in Prudoe Bay in Alaska.

The uppermost productive member of the Monterey Formations is the Diatomite that passes westward into the argillaceous Reef Ridge Shale. The Diatomite overlies the Brown Shale with the diagenetically defined boundary. The Brown Shale in turn overlies the Antelope Shale member of the Monterey. Cyclic bedding in the siliceous facies is a well documented phenomenon attributed to alternating deposition of detritus beds, clay, and biogenic beds (mostly diatoms; 75 million of these microscopic plants fill a cubic inch). The cycles span length-scales that range from a fraction of an inch to tens of feet, reflecting the duration of depositional phases from semi-annual to thousands of years.

The mineral composition of diatomaceous rocks can be depicted as a mixture of biogenic silica, detritus and shale. For example, the South Belridge diatomite has more biogenic silica, and the Lost Hills diatomite has more shale and sand. Depending on depth and temperature, the unstable biogenic or inorganic silica (Opal-A) dissolves and reprecipitates to form a metastable compound, Opal-CT (Brown Shale), that in turn dissolves and reprecipitates as microcrystalline quartz (Antelope Shale, Chert and/or Chalcedony).

The diatomaceous rocks are very porous (25-65%), rich in oil (35-70%), and almost impermeable (0.1-10 md). The high porosity and oil saturation, together with large thickness (up to 1000 ft) and area (up to a few square miles per field) translate into the gigantic oil-in-place estimates. Unfortunately, the low diatomite permeability makes efficient oil production very difficult, if not impossible, with current technology.[1]

To compensate for the low reservoir permeability, all wells in the diatomite must be hydrofractured. A typical well has 3-8 fractures with the wing span of 300 ft tip-to-tip. Wells are usually spaced along lines following the maximum in-situ stress every 330 ft (2½ acre), 165 ft (1¼ acre) or even 82 ft ($^5/_8$ acre). Thousands of hydrofractures have already been induced and thousands more may be created as new recovery processes, such as steamdrive on 5/8 acre spacing, become commercially viable. With so many hydrofractures so close to each other, it is crucial that we know their length, height, azimuth, dip, symmetry, conductivity and dynamics.

The hydrofractures in the diatomite can be imaged passively,[2-3] using the seismic energy released as the rock cracks and is propped open, and actively, using shear wave shadowing. In the case of passive imaging, the microseismic event arrival times are picked and inverted to find the event locations, which are then used to infer the hydrofracture geometry as a function of time. As in any arrival time based inversion, the calculated event locations are very sensitive to the errors in the picked arrival times and the choice of an "average" formation velocity.

We present the results of passive imaging of hydrofractures in two injectors in Shell's Phase II steamdrive pilot in South Belridge. We developed an inversion algorithm based on a modified conjugate gradient method with a constant velocity model (CVM). By using a layered shear velocity model and Monte Carlo simulations, we have delineated the limitations of CVM. Finally, to correct for the azimuthal variability of shear wave velocity in the diatomite, we calculated the distortion of conical waves from air gun blasts in a nearby logging observation well.

Experiment Description

Fig. 1 depicts a plan view of the Phase II steamdrive pilot in Section 29 of the South Belridge diatomite. Hydraulic fractures were induced in three treatment wells: producer 543P, followed by two steam injectors IN2U and IN2L. Wells IN2U and IN2L were perforated from 1110 to 1460 ft and from 1560 to 1910 ft, respectively. Well 543P was perforated in the lower zone between 1540 and 1890 ft. Results of hydrofracture imaging in 543P have been reported elsewhere.[2-3] Three dedicated microseismic observation wells, MO-1, MO-2, and MO-3, were strategically placed about the treat-

*Now with Fair Isacc Inc.

Original SPE manuscript received for review Dec. 1, 1994. Revised manuscript received Sept. 18, 1995. Paper peer approved Oct. 6, 1995. Paper (SPE 28383) first presented at the 1994 SPE Annual Technical Conference and Exhibition held in New Orleans, Sept. 25–28.

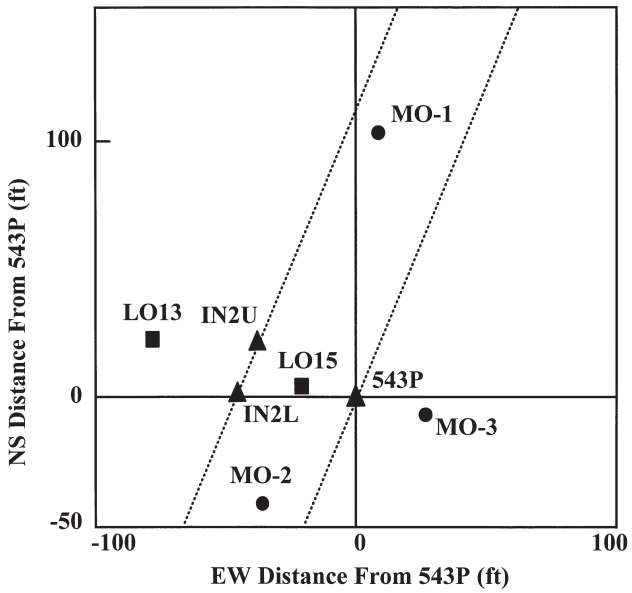

Fig. 1—Plan view of microseismic experiment in the South Belridge field.

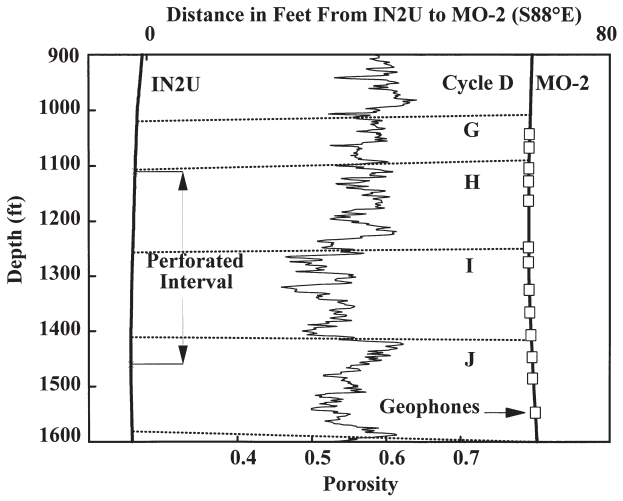

Fig. 2—Cross-sectional view of experiment site shown with porosity log and geologic layering.

ment wells. In each observation well, an array of three-component geophones was strapped onto the casing and cemented in place. The geophone stations were spaced every 20 ft over the entire diatomite column. A second array in MO-3 had geophones positioned every 5 ft over a 200-ft interval at the bottom of the diatomite. Vinegar *et al.*[2] provided a detailed description of the materials used in the construction of the geophone pods. **Fig. 2** is a cross-sectional view of the experiment site between IN2U and MO-2. Only the active geophones that span the perforated interval of IN2U are shown. The diatomite cycles and porosity log are also shown. Note that porosity jumps from 30 to over 60% across the top of the diatomite at a depth of about 900 ft.

LO13 is a logging observation well in which an air gun was fired for the purpose of shear-wave shadowing of the fracture in IN2U. These blasts also generated tube waves that proved invaluable in our analysis. A logging observation well LO15 and MO-3 were used to determine the formation shear velocity log by measuring the interwell seismic travel time. The velocity was found to range from about 1800 to 2300 ft/s.

The fracturing of IN2U consisted of a six-stage minifrac and a seven-stage main frac (**Table 1**). Only the main fracture was induced in IN2L. Generally, the pumping rate was higher with each subsequent stage of the minifracs and was significantly increased during the main frac. All mini frac stages were pumped with 2% KCl brine except the last one in which cross-linked 40 pound gel was used. Main fracs were pumped with 2% KCl brine, cross-linked 40 pound gel, and 20/40 Ottawa sand.

Data Acquisition

Fifty-six channels of data were recorded by Western Geophysical Downhole Seismic Services using a 60-channel DFS-V system with dual 9-track magnetic tape drives. Channel limitations restricted recording to approximately 18 geophones from each observation well during each fracturing stage. Thus, only the geophones spanning the perforated interval in the treatment well were used. The data were collected at a 1 ms sample rate in 16-second blocks separated by a 950 ms gap to allow for the DFS-V to reinitialize the recording sequence. Also, an LRS-1300 triaxial borehole tool was used to acquire the microseismic data in the treatment well. Over five hours of continuous recording time was required for each fracture treatment, resulting in almost 10 GB of data.

The data were band-pass filtered to eliminate 60 Hz electronic noise and low energy frequencies, thus improving the signal to noise ratio. We also used predictive deconvolution to help reduce any coherent noise signal. Despite this processing, we were able to detect the arrival of seismic energy only in the form of shear waves, as shown in **Fig. 3.** The hyperbolic move out of about 2000 ft/s identifies this shear wave arrival. We did not find any *P*-wave arrivals associated with the microseismic events that could be picked with confidence. Wills *et al.*[3] reported that compressional waves are highly attenuated in diatomite and that shear waves are produced with a much larger amplitude. We believe that our inability to detect *P*-wave arrivals was also because of their horizontal polarization, which inhibited *P*-wave detection by the vertical-component receivers. Unfortunately, analysis of the few horizontal-component channels was inconclusive as well.

When a microseismic event was found, the arrival times were picked by hand for each geophone. We feel that the time-consuming process of picking by hand resulted in greater accuracy of inversions for the microseismic event locations.

Inversion Algorithm

The reason for having three observation wells with multiple geophones was to allow for an accurate inversion of event locations by triangulation. An easy way to view such an inversion in two dimensions is to imagine growing circles at a constant rate about each observation well. The point where these circles intersect defines the

TABLE 1—FRACTURE DATA FOR IN2U AND IN2L

Stage	Starting Time	Volume (bbl)	Rate (bpm)	Fluid Type
Mini 1 (IN2U)	5:56	50.22	9.21	2% KCl brine
Mini 2	6:29	100.22	8.37	2% KCl brine
Mini 3	7:01	375.51	4.99	2% KCl brine
Mini 4	8:19	326.40	18.20	40 lb CLG
Mini 5	8:37	76.57	24.05	2% KCl brine
Mini 6	9:11	11.73	0.90	2% KCl brine
	next day			
Main 1 (IN2U)	10:27	76.30	22.12	2% KCl brine
Main 2	10:49	51.25	23.29	40 lb CLG
Main 3	10:51	193.43	26.26	40 lb CLG and OS
Main 4	10:59	297.39	26.28	40 lb CLG and OS
Main 5	11:10	416.07	26.31	40 lb CLG and OS
Main 6	11:26	432.49	26.29	40 lb CLG and OS
Main 7	11:42	43.40	25.53	40 lb CLG
Main 1 (IN2L)	5:51	201.75	25.06	2% KCl brine
Main 2	6:10	69.28	23.48	CLG
Main 3	6:13	193.95	26.21	CLG and OS
Main 4	6:20	295.72	26.13	CLG and OS
Main 5	6:32	460.05	26.14	CLG and OS
Main 6	6:49	499.35	26.12	CLG and OS
Main 7	7:08	55.73	25.72	2% KCl brine

CLG = Cross-linked gel
OS = 20/40 Ottawa sand

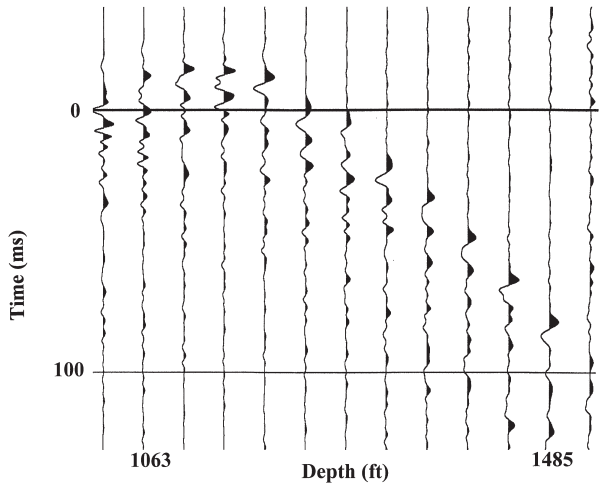

Fig. 3—Shear wave arrival at MO-2 recorded by the vertical component of the geophones (note hyperbolic moveout).

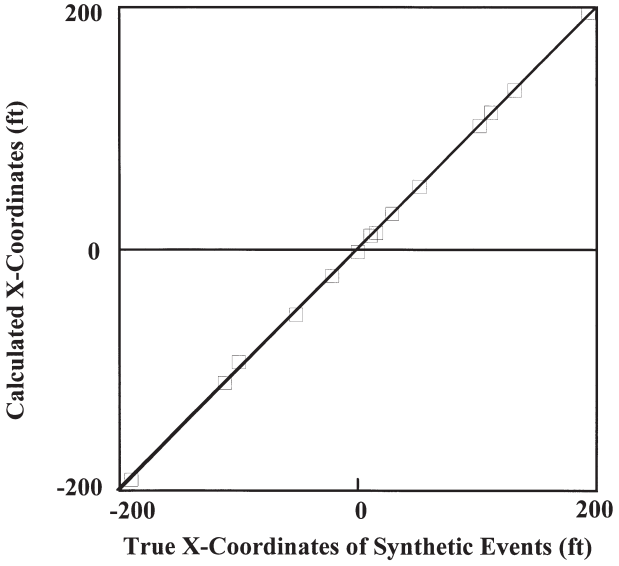

Fig. 4—Each square represents the X-coordinate calculated by the location algorithm vs. the true X-coordinate of the corresponding synthetic event.

event location. We developed a five-dimensional inversion algorithm that uses a modified conjugate gradient method to minimize an objective function:

$$\sum_{i=1}^{\#geophones}\left[\sqrt{(x_i-x_{ev})^2+(y_i-y_{ev})^2+(z_i-z_{ev})^2}-v_{ev}(t_i-t_{ev})\right]^2 \quad \ldots\ldots\ldots\ldots\ldots\ldots\ldots (1)$$

for each event, *ev*. The unknowns here are x_{ev}, y_{ev}, z_{ev}, t_{ev} and, if desired, v_{ev}.

The algorithm can be executed in one of two modes. In Mode #1, the single velocity used for the inversion is picked from the interwell shear velocity log for the depth of the earliest shear wave arrival at each observation well. In Mode #2, the single best velocity is calculated as a part of minimizing Eq. 1, using a separate Golden Section Search[4] in the velocity dimension (because time and velocity enter Eq. (1) as a product). In either case, the chosen velocity is assumed to be uniform in all directions and constant with depth. Thus, the algorithm *always* assumes a homogeneous or constant velocity model (CVM) during the inversion, regardless of the execution mode.

To test the algorithm, synthetic event locations were selected at various locations and depths throughout the test site, inside and outside of the geophone network. The shear wave travel times to each geophone were computed for a uniform medium of a specified velocity. The arrival times were then inverted in Mode #2, and the calculated locations compared with the selected ones. **Fig. 4** shows the results of the calculated *x*-coordinates versus the selected *x*-coordinates. The inversion is accurate to within one foot. Similar plots for the other calculated parameters (*y*-coordinate, depth, origin time, and velocity) reveal the same precision. After thorough testing, we feel that this algorithm is superior to the standard least square fit with Gaussian elimination, which suffers from ill conditioning and round off errors.

Validity Test for Inversion Algorithm. Having established that the inversion algorithm worked numerically in a homogeneous medium, we needed to test its capacity to invert field data. A depth-dependent, but otherwise constant shear velocity model is rarely a good representation of a layered and heterogeneous rock. Seismic waves propagating through such a rock are subject to velocity changes that result in ray-bending. On the other hand, a constant velocity model assumes straight ray paths, and it is necessary to resolve the systematic error incurred when inverting real data with such a model.

To find this error, we first developed a horizontally layered, shear wave velocity model, using the interwell velocity and bulk density logs. The model velocities and layering were chosen to represent the diatomite formation as accurately as possible and are shown in **Fig. 5. Fig. 6** compares two sets of arrival times, one generated with our layered model and the other from a real microseismic event. The approximate agreement between these and other arrival times con-

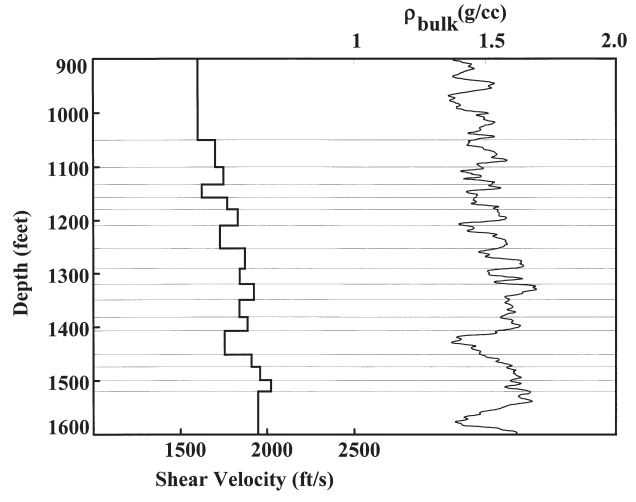

Fig. 5—Layers with respective shear velocities for layered model shown with bulk density log.

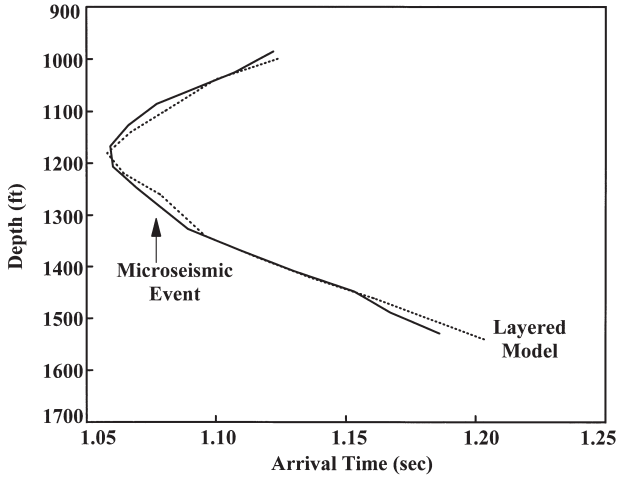

Fig. 6—Arrival times comparison.

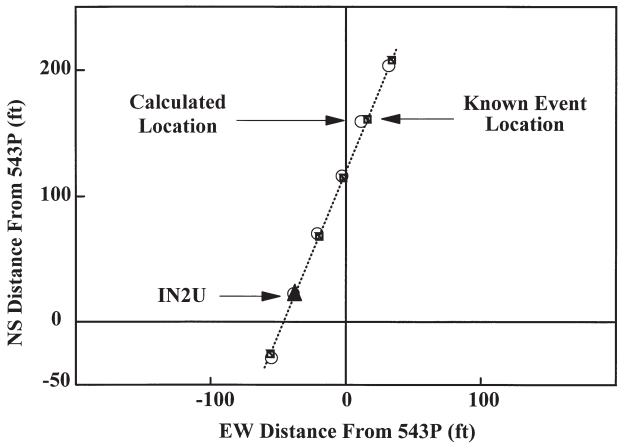

Fig. 7A—Known vs. calculated locations (1200 ft).

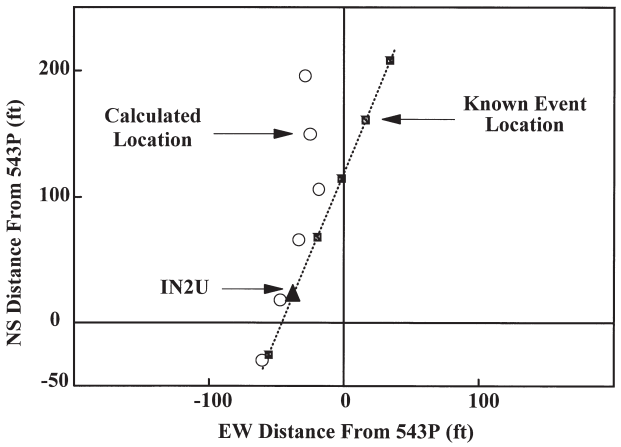

Fig. 7B—Known vs. calculated locations (1400 ft).

vinced us that our layered model was a reasonable representation of the diatomite.

Next, we assumed *known* synthetic event locations at various depths along the estimated hydrofracture plane in IN2U. The shear wave travel times to each geophone were then computed from the *layered* model. These arrival times were in turn inverted with CVM in Mode #1, and the calculated locations were compared with the known ones. **Figs. 7A and B** show the results of this comparison in plan view for the events at 1200 and 1400 ft, respectively.

The calculated locations may seem acceptable, but they still result from inverting ideal, *error-free* arrival times, which are hardly typical of field data. The arrival times of real seismic events are subject to various errors. There is error because of the recording equipment, noise in the seismic signal, and the actual picking of the arrival times. Unfortunately, these errors are difficult to decouple.

To test the validity of inverting real data with CVM, we had to introduce an element of error into the arrival times computed from the layered model. Accordingly, we perturbed the arrival time at every geophone by a random factor of the order of four milliseconds. This random factor, which is approximately one third of the average period for the real shear wavelengths in our data, was to account for all errors. Inverting the arrival times after each of 500 perturbations yielded an oriented ellipsoid of uncertainty for the calculated locations in Figs. 7A and B.

Figs. 8A and B show the uncertainty "clouds" around the calculated locations, together with the *known* synthetic locations. These plots are more significant than those in Figs. 7A and B, because the calculated location for a real microseismic event corresponds to *any* of the event locations composing the uncertainty ellipsoid. The error associated with inverting real data using a homogeneous model is represented by the distance between the uncertainty cloud and the specified location. If the cloud encompasses the specified location, then such an inversion is valid for that location, given appreciable errors induced by well geometry, geophone spacing, and all other errors discussed above. If the specified location falls outside of the cloud, then inverting with a homogeneous model is insufficient for that location, and a vertically variable velocity inversion (a more difficult task) must be performed.

Conditional Validity. In Fig. 8A, the uncertainty ellipsoids are in good agreement with the specified locations at all distances from the treatment well. However, in Fig. 8B they compare favorably near the treatment well but get progressively worse with distance away from the borehole. We believe that this diminished accuracy is related to the vertical location of the synthetic events. At 1400 ft, the shear wave velocity has a higher gradient than at 1200 ft, which could explain why our accuracy is poorer at 1400 ft. The variation in shear velocity is more important than its magnitude. A larger gradient leads to more seismic ray bending and greater uncertainty. In addition, events farther away from the geophone wells are more prone to ray bending, explaining why accuracy diminishes with distance.

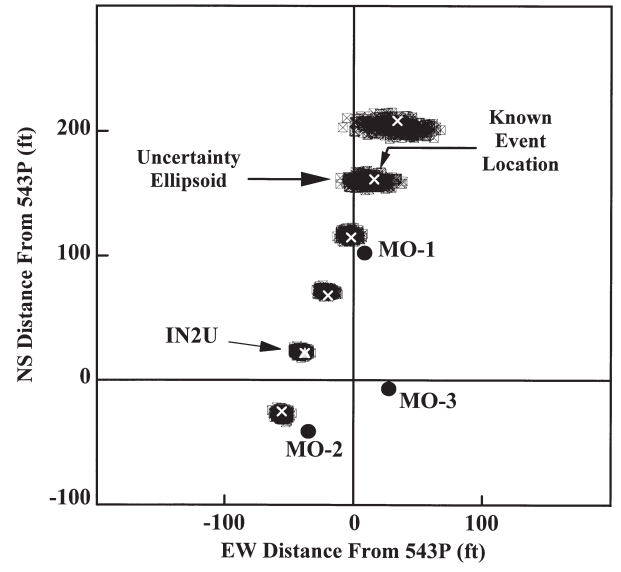

Fig. 8A—Known locations vs. uncertainty ellipsoids (1200 ft).

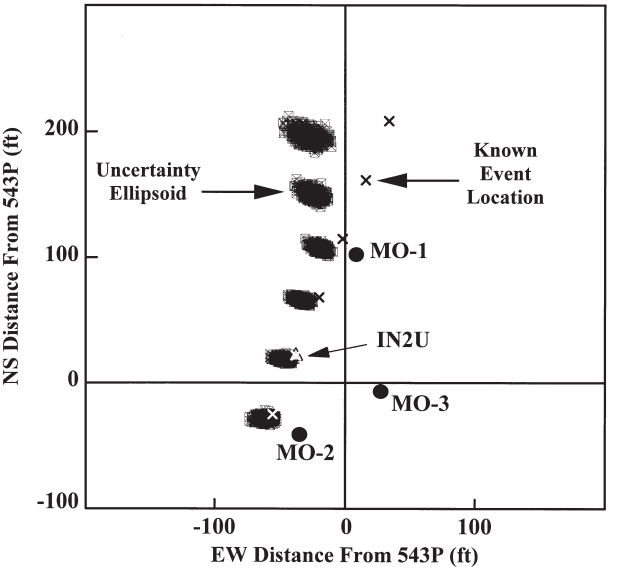

Fig. 8B—Known locations vs. uncertainty ellipsoids (1400 ft).

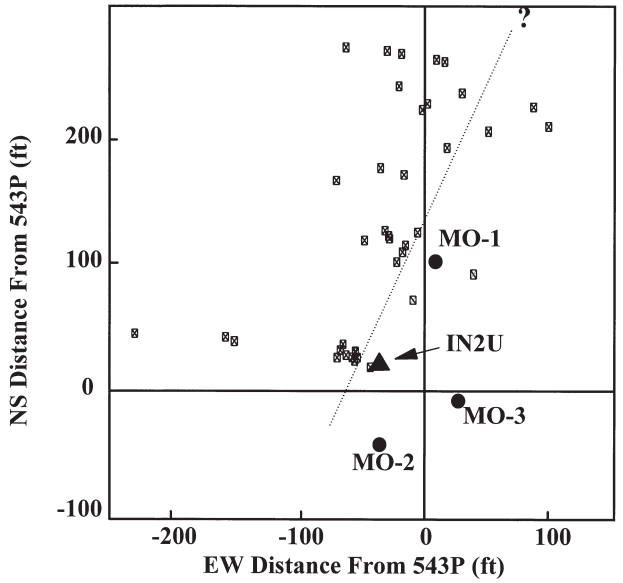

Fig. 9—IN2U microseismic event locations using constant velocity model.

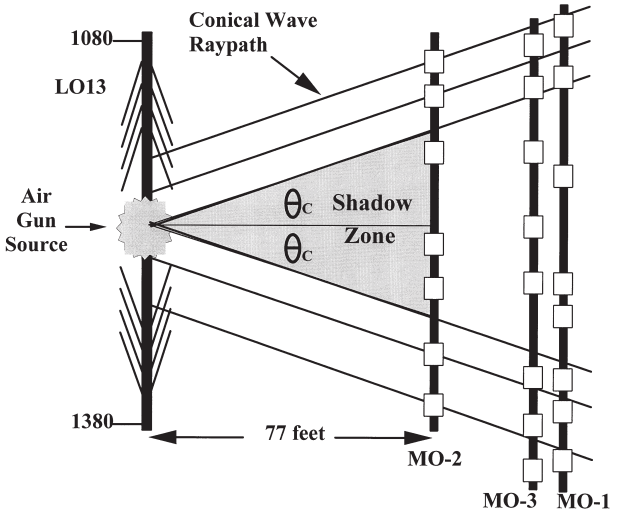

Fig. 10—Conical wave generation and propagation.

Initial Event Locations for IN2U

After determining the accuracy and limitations of our inversion method, we proceeded to invert the arrival times of real microseismic events. The search through all the IN2U hydrofracture data resulted in the detection of about 80 direct arrivals. Unfortunately, half of these were conical waves caused by the air gun shots that were used for the shear wave shadowing analysis.[2] We picked the arrival times for all the microseismic events and inverted them using CVM.

Fig. 9 is a plan view showing the calculated event locations for the microseismic events. The locations are much more dispersed than we expected, and it is difficult to define any fracture plane at all. Also, the fracture is asymmetrical, extending almost entirely northeast of IN2U. These results led us to question again the validity of our inversion routine, but from a different perspective.

The validity tests described above showed that inverting real data with CVM is acceptable for our purposes. However, for the South Belridge diatomite, *lateral* variability of shear velocity may exist and must be taken into account when inverting for the microseismic event locations. In fact, with only three geophone wells, azimuthal variation could be a more significant source of error than vertical variation. Thus, we devised a method to detect directional changes in shear velocity in the diatomite. The conical waves from the air gun blasts in LO13, which had originally been considered an unwanted noise, were now viewed as a potentially useful tool to estimate the shear wave velocity between LO13 and the three observation wells.

Conical Waves

Generation and Propagation. Conical waves are frequently encountered in vertical seismic profiling (VSP). An air gun blast causes a fluid disturbance within the well that emits tube waves which travel up and down the borehole, away from the air gun.[5-6] As the tube waves propagate, they diffract into the formation as conical wave fronts if the tube wave velocity exceeds the velocity of the adjacent formation.[2,7] For our test site, the tube wave velocity is greater than the diatomite's shear velocity but less than its compressional velocity; hence, we can detect only shear conical waves in our data.[8] The conical waves emerge into the formation at an angle θ with respect to the perpendicular to the borehole, where

$$\Theta = \sin^{-1}\left[\frac{V_s(z)}{V_t(z)}\right]. \quad \ldots\ldots\ldots\ldots\ldots\ldots\ldots\ldots\ldots\ldots (2)$$

$V_s(z)$ is the depth-dependent shear velocity of the formation, and $V_t(z)$ is the tube wave velocity. The angle in our case varies from about 27° to 45° and is more sensitive to V_s than to V_t. **Fig. 10** illustrates the ray paths taken by the conical waves from LO13 to the observation wells. Note the shadow zone, equal to 2θ, separating the conical waves generated by the up- and downgoing tube waves. Consequently, only geophones whose depths are greater or less than

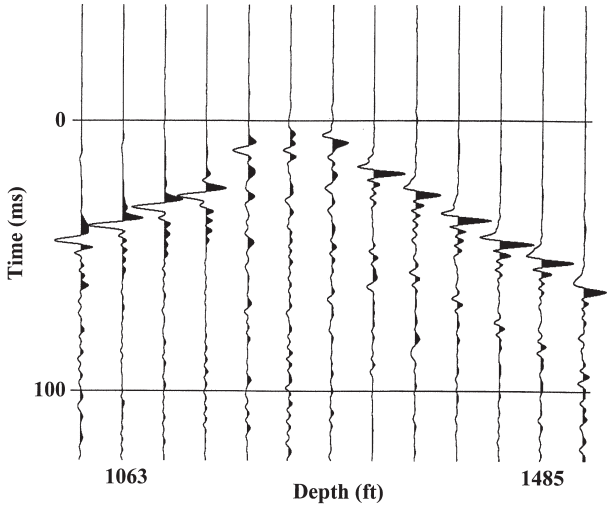

Fig. 11—Conical wave arrival at MO-2 recorded by the vertical component of the geophones (note shadow zone).

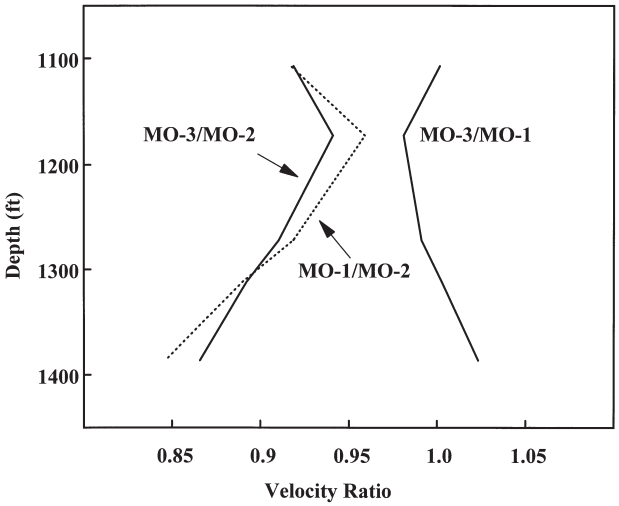

Fig. 12—Relative shear wave velocities.

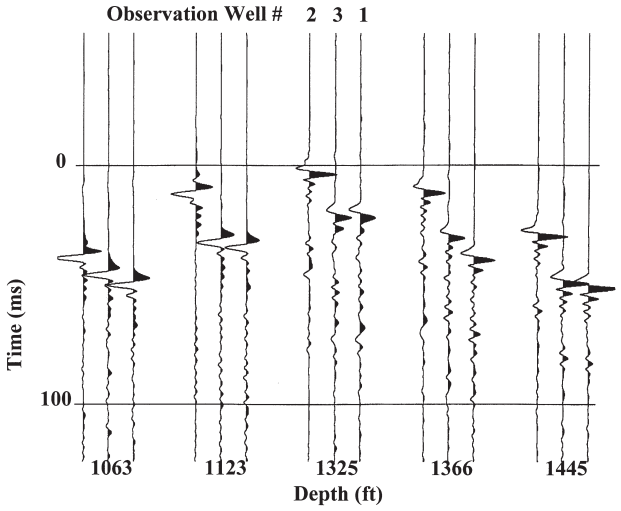

Fig. 13—Conical wave arrivals corrected for both depth and distance.

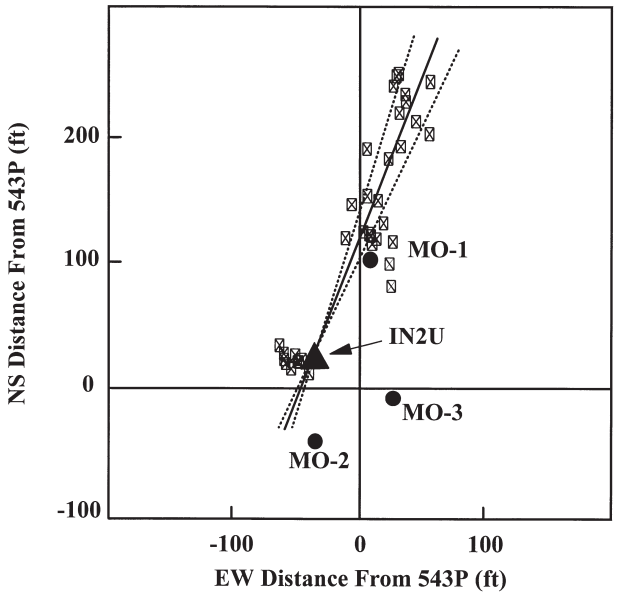

Fig. 14—IN2U microseismic event locations using relative velocities.

the depth of the air gun by an amount equal to $r\tan\theta$, where r is the radial distance from LO13, will record strong conical wave arrivals.

The zero frequency approximation of the tube wave velocity is[9]:

$$V_t(z) = \left\{\rho_f\left[\frac{1}{B_f} + \frac{1}{V_s^2(z)\cdot\rho_r + Eh/d}\right]\right\}^{-\frac{1}{2}}, \quad \ldots\ldots\ldots\ldots (3)$$

where ρ_f is the well fluid density; B_f is the bulk modulus of the well fluid; $V_s(z)$ is the depth-dependent formation shear velocity; ρ_r is the bulk density of the formation; and E, h, and d are the Young's modulus, wall thickness, and inner diameter of the well casing, respectively. The tube wave velocity was computed to be about 4300 ft/s and is most sensitive to ρ_f. Because conical waves attenuate as the square root of the distance from the source well, they can be recorded over large distances away from the borehole.[5] **Fig. 11** shows an example of a conical wave arrival in one of the observation wells. The three earliest arrivals are direct shear waves that are visible only because they are within the conical wave's shadow zone. Outside the shadow zone, strong conical wave arrivals can be seen which completely scale out the direct shear wave. The linear moveout at an apparent velocity equal to the tube wave velocity characterizes the conical wave. Contrast Fig. 11 with the shear wave arrival from a microseismic event in Fig. 3, which has hyperbolic moveout and a slower apparent velocity.

Use of Conical Waves to Estimate Relative Shear Velocities. The *relative* variation of shear velocity with azimuth was of greater interest than the velocity magnitudes themselves. Therefore, we specified a shear velocity in one direction as a reference. We chose the direction from LO13 to MO-2 as our reference direction. Five conical wave ray paths, each being emitted from LO13 at a different depth, were then determined in such a way as to intersect MO-2 at a specific geophone depth while intersecting MO-1 and MO-3 at depths where a geophone was positioned nearby (cf. Fig. 10). First, a reference shear velocity was taken from the interwell log and assigned to each ray path according to the ray path's depth. The emergent angles of the conical wave ray paths from LO13 were then calculated using Eqs. (2) and (3) above. We assumed straight ray paths for the conical waves. The three geophones for each ray path were grouped together for the analysis.

The modeled travel time of the conical wave to MO-2 was found by dividing the straight ray distance, r_2, from LO13 to MO-2 by the reference shear velocity, V_r. The origin time, t_o, of the air gun shot was then calculated by subtracting the modeled travel time from the picked arrival time, t_{a2}, at the geophone in MO-2:

$$t_o = t_{a2} - \frac{r_2}{V_r}. \quad \ldots\ldots\ldots\ldots (4)$$

The arrival times, $t_{a1,3}$, at the geophones in MO-1 and MO-3 were corrected for the difference in depth, $\Delta z_{1,3}$, between the intersection of the chosen conical wave ray path with these observation wells and the nearest geophone:

$$t_{c1,3} = t_{a1,3} \pm \frac{\Delta z_{1,3}}{V_t}, \quad \ldots\ldots\ldots\ldots (5)$$

where $t_{c1,3}$ is the corrected arrival time in MO-1 or MO-3, and V_t is the tube wave velocity. This correction assumed parallel ray paths for conical waves emanating at depths that were very close to the depths of the five chosen ray paths. Subtracting the origin time, t_0, from the corrected arrival times at MO-1 and MO-3 gave the travel times of the conical waves to those wells. The relative velocities, $V_{rel1,3}$, were then computed by dividing these travel times into the straight ray distances, $r_{1,3}$, to MO-1 and MO-3

$$V_{rel1,3} = \frac{r_{1,3}}{t_{c1,3} - t_o}. \quad \ldots\ldots\ldots\ldots (6)$$

Since the relative velocities were calculated with respect to the reference velocity in the MO-2 direction, we divided them by the reference velocity to get shear velocity ratios. **Fig. 12** shows the shear velocity ratios as a function of the depth at which the five chosen ray paths emerged from LO13. Note that the velocity towards MO-2 is about 10% greater than that towards MO-1 and MO-3 (ratios of 0.9). Failing to account for such a difference in shear velocity when performing inversions can drastically alter the microseismic event locations.

Evidence confirming that the shear velocity does indeed vary with direction can be seen in **Fig. 13,** which shows the arrival of a conical wave at each of the fifteen geophones. The three receivers for each of the five ray paths have been grouped together, and the arrivals at the geophones in MO-1 and MO-3 have been corrected for depth using Eq. (5) and distance:

$$\Delta t_{1,3} = \frac{r_{1,3} - r_2}{V_r}, \quad \ldots\ldots\ldots\ldots (7)$$

where $t_{1,3}$ is the time correction for the extra radial distance to MO-1 and MO-3. In other words, Fig. 13 shows what the relative arrival of a conical wave would be at a specific geophone in each observation well if the three receivers were positioned at exactly the same depth, and the distances from LO13 to MO-1, MO-2, and MO-3 were equal. All five geophone groups are shown. If the shear velocity in the diatomite was the same in all directions, the three arrival

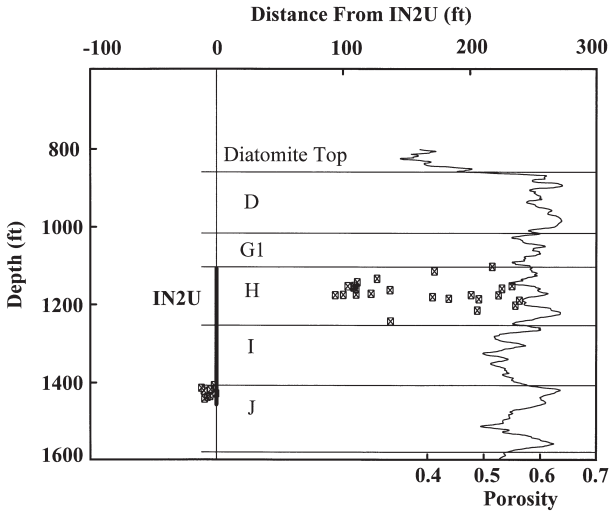

Fig. 15—Side view of IN2U fracture zone (N69°W).

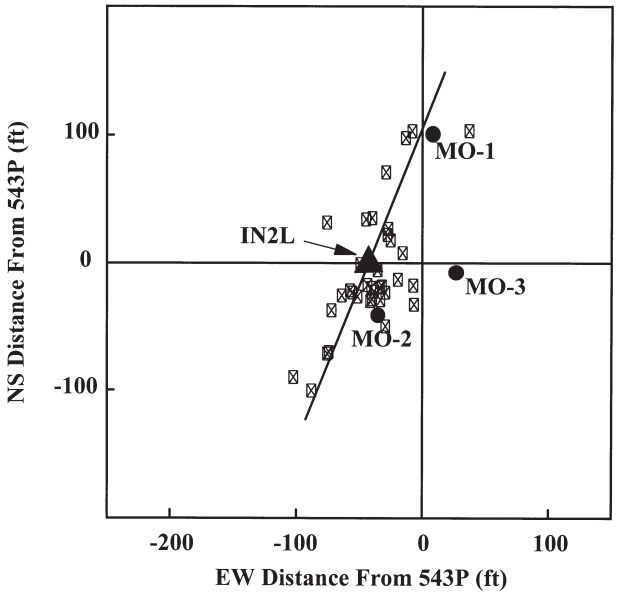

Fig. 16—IN2L microseismic event locations with relative velocities.

times within each group would be synchronous. However, Fig. 13 clearly shows that the arrival time is earlier for the MO-2 geophone in all five groups. Thus, the shear velocity is faster towards MO-2 than towards MO-1 and MO-3 for all five depths.

Improved Event Locations for IN2U

The extent of deformation of conical waves allowed us to estimate the *lateral* variability of shear velocity in the vicinity of IN2U. **Fig. 14** is a plan view of the new locations of the microseismic events, after inverting in Mode #1, with the aid of velocity multipliers. We were pleased to see that these locations have collapsed onto a well-defined fracture plane. This plane is almost vertical and strikes approximately N21°±4°E. The azimuth from a tiltmeter survey by Applied Geophysics, Inc. was N19.4°±4°E. Contrasting Fig. 14 with Fig. 9 reveals the magnitude of improvement in the event locations as a result of accounting for the azimuthal variation in shear velocity. Fig. 14 also confirms that the hydrofracture extended asymmetrically about IN2U. Its NE wing was about 230 ft long and its SW wing was no more than 30 ft long. Another intriguing aspect of the fracture, however, is shown in **Fig. 15.** This side view reveals that the asymmetrical wings occurred at two different depths. There are actually two different fractures—a long NE wing at a depth of about 1200 ft and a short SW wing at about 1400 ft. Both depths correspond to the highest permeabilities in the diatomite layers near IN2U. The lack of symmetry of the fracture wings in IN2U indicates significant reservoir heterogeneity or nonuniform pore pressure. This finding differs from those reported in the literature, e.g. Stewart *et al.*[10]

Event Locations for IN2L

The deep hydrofracture was induced in IN2L, the second steam injector. After picking the arrival times, we inverted for the microseismic event locations in Mode #1, using the relative velocity multipliers of 1.20 for MO-1 and 0.87 for MO-2. The azimuthal variation in shear wave velocity around IN2L could be large as a result of hydrofracturing in 543P over the same vertical interval and only 40 ft east (Fig. 1). As reported in [2], IN2L was next to the disturbed formation around the hydrofracture in 543P. There were no air gun shots during fracturing of IN2L, and the velocity multipliers used above were calculated from the conical wave events in IN2L itself. **Fig. 16** shows the results of the inversion in plan view. Again, we have a fairly well-defined fracture plane that strikes approximately N21°E for this particular set of multipliers (without the multipliers the fracture azimuth was an unacceptable N35°E).

Other conical wave events seem to indicate that the fracture azimuth is closer to N25°E—N30°E, and we continue to refine our analysis. The microseismic analysis of the hydrofracture in 543P yielded[2-3] an azimuth of N26°±6°E. This time the hydrofracture is symmetrical about IN2L and both wings are approximately 130 ft long. A side view of the hydrofracture in IN2L is shown in **Fig. 17.** We can see that both fracture wings are at a depth of about 1650 ft, suggesting that there is only one major fracture in IN2L. There is also a short, symmetrical fracture at about 1850 ft depth, extending no more than 10 ft in each direction.

Temperature Data

Fig. 18 shows the locations of the Phase I and Phase II steamdrive pilot injectors, producers and observation wells. Note that the Phase I hydrofractures have azimuths of about N15°E, in agreement with other field data. As the upper cycles of the diatomite have lower permeabilities than the bottom ones, the drawdown from producer 543H resulted in a steeper pressure gradient that attracted the new hydrofracture in IN2U. Similarly, the more significant,[1] but slowly occurring *lateral* extensions of the hydrofracture in IN2U are dominated by the attraction from a full-interval producer 543N, whereas those in IN2L by producer 543P, completed only in the lower zone. In short, both injection hydrofractures are dynamic systems that evolve with time, depending on the local stress field that in turn is influenced by the pore pressure. The early behavior of these hydrofractures, however, is closely related to their original shape and extent and can be verified by the initial temperature surveys in the observation wells.

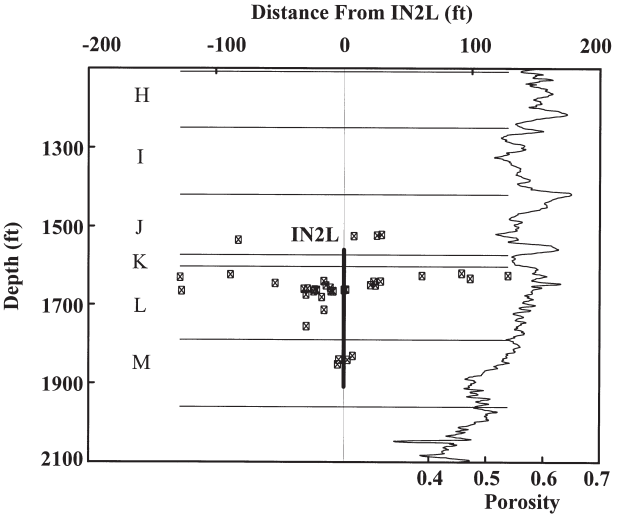

Fig. 17—Side view of IN2L fracture zone (N69°W).

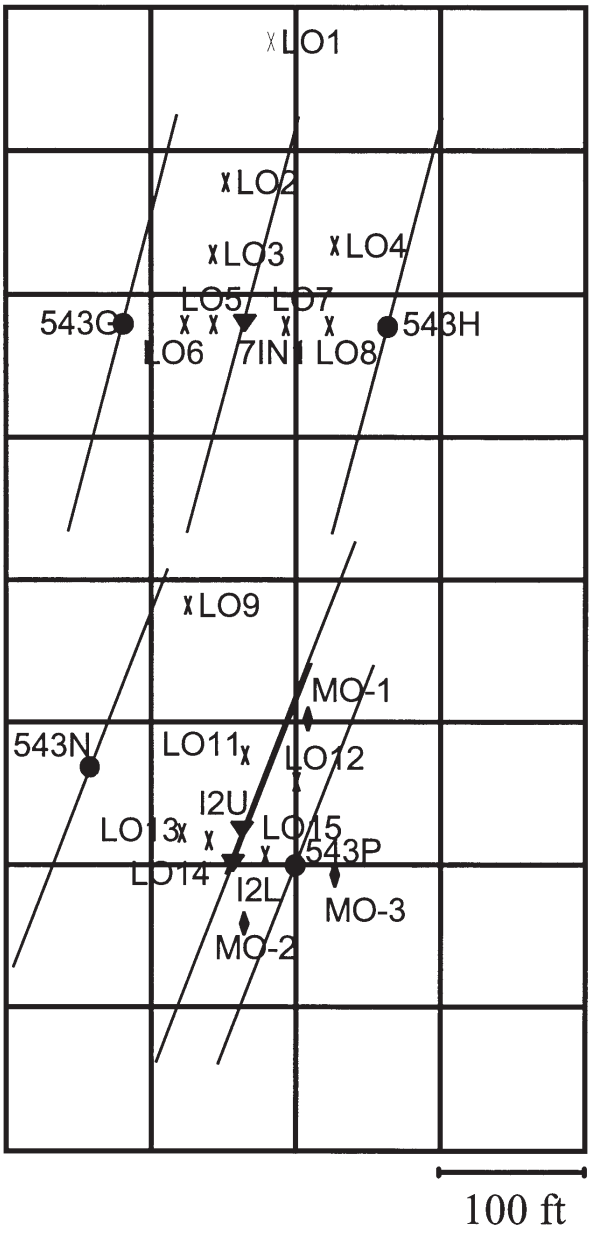

Fig. 18—Plan view of the Phase I and Phase II steam drive pilots.

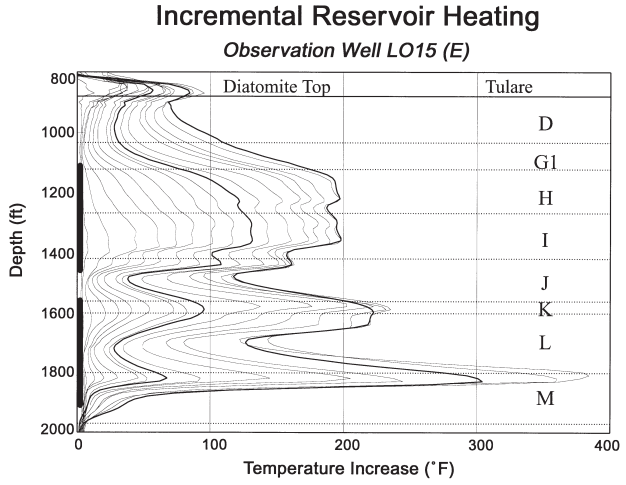

Fig. 19—Square-root-of-time interpolation of temperature surveys in observation well LO15.

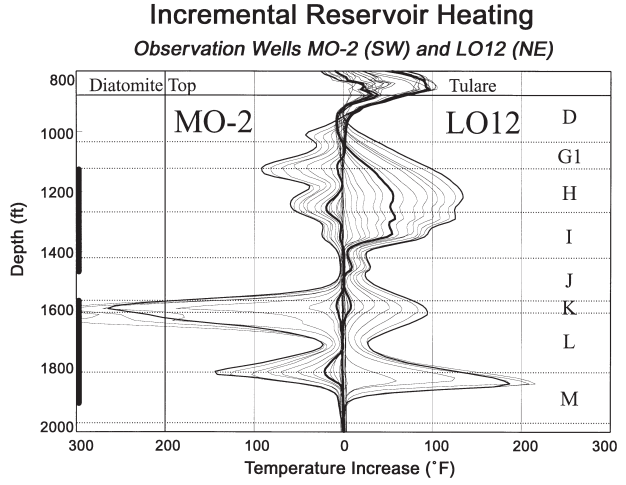

Fig. 20—Square-root-of-time interpolation of temperature surveys in wells MO-2 and LO12.

It is well known that in linear, transient and nonisothermal flow of steam, the reservoir pressure and temperature are governed by a nonlinear pressure diffusion equation coupled with a linear heat conduction equation, and vary approximately as the square root of time.[11,12] Therefore, if there is no deviation from linear flow of mass and heat, the temperature profiles in an observation well should be spaced uniformly when interpolated in equal increments of the square root of time elapsed on steam injection.

Observation well LO15 is located 23 ft east from both injectors. **Fig. 19** shows a square-root-of-time interpolation of temperature surveys in this well between 200 and 1400 days of steam injection. The two thick surveys are at 770 and 1400 days. Well LO15 is dominated by the pulverized formation close to the injectors—not the hydrofracture planes far from the injectors—and has responded to steam injection into both upper hydrofractures at 1200 and 1400 ft and both lower hydrofractures at 1650 and 1850 ft.

Geophone/observation well MO-2 is located 63 ft SE from IN2U and 44 ft SE from IN2L. Observation well LO12 is located 53 ft NE from IN2U and 71 ft NE from IN2L. Both observation wells are about 20 ft east of the injector hydrofracture planes. Therefore, one would expect these wells to respond similarly to steam injection. If both wings of the hydrofractures were symmetrical, the response of well MO-2 to IN2U would be slightly *retarded* relative to LO12. Conversely, the response of MO-2 to IN2L would be *accelerated* relative to LO12. However, the *magnitude* of both responses should be similar. The temperature increases in MO-2 and LO12 are shown in **Fig. 20.** Note that after 770 days of steam injection (the first thick survey), well MO-2 had shown almost no heating across the upper injection interval, whereas LO12 heated uniformly up to 60ºF. Even after 1400 days of steam injection and several fracture extensions, the reservoir heating at MO-2 lagged significantly that at LO12. Also note that there is no heating in both wells at 1400 ft, suggesting that the lower hydrofracture in IN2U never increased its length. This is the most direct proof of our conclusions from the microseismic imaging of the hydrofracture in IN2U. Interestingly, almost no response to IN2L was seen at both wells for the first 770 days of steam injection. Thereafter, the heating accelerated more in MO-2 at 1650 ft, but more in LO12 at 1850 ft. This suggests that (1) new flow channels, perpendicular to the hydrofracture plane, opened and (2) the deepest hydrofracture increased its length many-fold. Both heated depths correspond to the microseismic activity.

Conclusions

Two hydrofractures in the South Belridge Diatomite were imaged passively using the seismic energy released during fracture propagation:

1. The azimuth of both hydrofractures was about N21° ± 4°E.

2. In each treatment well, there were initially two separate hydrofractures at two different depths that corresponded to the diatomite layers with highest permeabilities.

3. The IN2U hydrofractures were asymmetrical. Initially, the upper NE wing at 1200 ft was 230 ft long, whereas the lower SW wing at 1400 ft was only 30 ft long. The lower wing never grew significantly.

4. Asymmetry of a new hydrofracture is likely to be caused by the areal nonuniformity of pore pressure around this hydrofracture.

5. The IN2L hydrofractures were symmetrical and their wings were initially 130 ft long at 1650 ft and 10 ft long at 1850 ft. The lower wings increased their length many-fold during steam injection.

6. The above conclusions agree with temperature surveys in the surrounding observation wells.

7. Our sensitivity analysis indicates that the lateral uncertainty in the microseismic event locations is usually ± 20 ft while the vertical one is ± 2-5 ft.

8. The microseismic data are scattered around the most likely fracture planes within ± 20-25 ft. This means that the existence of the disturbed "process zones" around the hydrofractures is neither supported nor rejected by the data.

The hydrofracture in IN2U was very different than that in IN2L. Therefore, the diatomite properties can change dramatically with depth and time, and this has implications for the implementation of steamdrive on a $^5/_8$ acre spacing.

Acknowledgments

We would like to thank Shell Development Company for releasing the unique hydrofracture imaging data set from the Phase II pilot to Dr. Patzek. Subsequently, Shell Western E&P, Inc. released to Dr. Patzek the temperature log data from the Phase II pilot. This work was supported entirely by the unrestricted research gifts from Shell Development Company, BP and Chevron to Dr. Patzek. We would also like to thank D. Schwartz and M. Johnston of Shell Western E&P, Inc. for their help. Also, valuable input from G. Sorrells and R. Adair of Teledyne Geotech, Inc. is gratefully acknowledged. Finally, we thank PV Technologies, Inc. for donating computer time and data visualization software to interpret the temperature logs.

References

1. Patzek, T.W.: "Surveillance of South Belridge Diatomite," paper SPE 24040, *Proc.,* 1992 SPE Western Regional Meeting, Bakersfield, CA, March 30–April 1, 171.
2. Vinegar, H.J. *et al.*: "Active and Passive Seismic Imaging of a Hydraulic Fracture in Diatomite," *JPT* (Jan. 1992) **44,** 28.
3. Wills, P.B. *et al.*: "Active and Passive Imaging of Hydraulic Fractures," *Geophysics: The Leading Edge of Exploration* (July 1992) **11,** 15.
4. Press, W.H. *et al.*: *Numerical Recipes in C: The Art of Scientific Computing*, Second Edition, Cambridge U. Press, Cambridge (1992) 397–402.
5. White, J.E.: *Seismic Waves: Radiation, Transmission, and Attenuation*, McGraw-Hill, Inc., New York City (1965).
6. Cheng, C.H. and Toksoz, M.N.: "Generation, Propagation and Analysis of Tube Waves in a Borehole," *Vertical Seismic Profiling, Part B: Advanced Concepts*, Geophysical Press, London (1984) **14B,** 276.
7. Meredith, J.A.: "Numerical and Analytical Modeling of Downhole Seismic Sources: The Near and Far Field," PhD thesis, Massachusetts Institute of Technology (1990).
8. Ilderton, D.C. *et al.*: "Microseismic Imaging of Hydrofractures with the Aid of Conical Waves," paper DP1.2, Expanded Abstracts of the 1993 SEG Annual Meeting and Intl. Exposition, Washington D.C., Sept. 26–30, 267.
9. Hardage, B.A.: *Crosswell Seismology and Reverse VSP*, Geophysical Press, London (1992) **1,** 147.
10. Stewart, L., Cassell, B.R., and Bol, G.M.: "Acoustic-Emission Monitoring During Hydraulic Fracturing," *SPEFE* (June 1992) **7,** No. 2, 139.
11. Carlslaw, H.S. and Jaeger, J.C.: *Conduction of Heat in Solids*, First Edition, Oxford U. Press, Oxford (1946) 50–132, reprinted in 1989.
12. Kovscek, A.R. and Patzek, T.W.: "Evaluation of Rock/Fracture Interactions During Steam Injection Through Vertical Hydrofractures," paper SPE 29622, *Proc.,* 1995 SPE Western Regional Meeting, Bakersfield, CA, March 8–10, 93.

SI Metric Conversion Factors

bbl	$\times 1.590$	E−01	= m
cycles/sec	$\times 1.0$*	E+00	= Hz
ft	$\times 3.048$	E−01	= m
°F	(°F − 32)/1.8		= °C
in.^{3}	$\times 1.638\ 706$	E+01	= cm^3
lbm	$\times 4.536$	E−01	= kg
md	$\times 9.869\ 233$	E−04	= μm^2

*Conversion factor is exact.

SPEFE

David C. Ilderton is a production programmer for Fair Isacc Inc. in San Rafael, CA. His current interests include seismic imaging of hydraulic fractures in low permeability formations. He holds a BS degree in geophysics from the U. of California, Santa Barbara and an MS degree in materials science and mineral engineering from the U. of California, Berkeley. **Tad W. Patzek** is an associate professor of petroleum engineering at U. of California, Berkeley. Previously, he worked for Shell Western E&P and in the Enhanced Recovery Research Dept. of Shell Development. His research activities include 3D modeling of foam flow in porous media with the population balance method; diffusion stability of stationary foams in porous media; the development of a finite-difference simulator of multiphase, multicomponent, nonisothermal flow in porous media; the use of steam to clean hydrocarbon spills; micro-earthquake imaging of massive hydrofractures; neural network models of fluid injection and withdrawal in tight rock; and inverse modeling of steam injection into diatomite. He holds a PhD degree in chemical engineering from Silesian Technical U., Poland. **James W. Rector** is an assistant professor of applied seismology at U. of California, Berkeley. Previously, he worked for Tomex Corp. developing seismic acquisition and processing technology to utilize drill bit vibrations as a downhole seismic source. He also developed drill bit source technology with Western Atlas Intl. His current research interests include crosswell reflection imaging, 3D VSP imaging, single-well profiling, and fracture/void detection using seismic scattering theory. He holds a BA degree in mathematics from the U. of Wisconsin, Madison, an MS degree in exploration geophysics, and a PhD in geophysics, both from Stanford U. **Harold J. Vinegar** is a senior staff physicist with Shell Development Co. in Houston. His research interests are in shaly sand evaluation, electromagnetic logging, enhanced recovery processes, CT and NMR imaging, and environmental remediation. He holds a BA degree from Columbia U. and MA and PhD degrees in physics from Harvard U.

Ilderton Patzek Rector Vinegar